


Theoretical understanding of Compton scattering-based reconstruction-free anatomical imaging method

Yuya Onishi^{✉*} and Ryosuke Ota^{✉†}

Central Research Laboratory, Hamamatsu Photonics K.K., Hamamatsu, Japan

 (Received 18 March 2024; revised 3 July 2024; accepted 23 July 2024; published 16 August 2024)

A reconstruction-free anatomical imaging algorithm that localizes the Compton scattering of annihilation γ rays within an object using ultrafast time-of-flight information and provides an anatomical cross-section image without tomographic reconstruction has been previously proposed. However, the spatial performance of generated images remains unclear. This study introduces a theoretical understanding and supporting simulation results of a Compton scattering-based reconstruction-free anatomical imaging method. First, we provide the exact algebraic solution, which was solved approximately in a previous study. Using the algebraic solution, the system performance can be quantitatively estimated via total differentiation. Total differentiation indicated that the difference in the path lengths of annihilation γ rays, which can be theoretically interpreted as the Compton scattering angle in an object strongly impacting the spatial resolution of the anatomical image. Monte Carlo simulations demonstrated that the spatial resolution of the generated images is improved by selecting events with large Compton scattering angles, which is consistent with the theory derived based on the algebraic solution. Furthermore, the use of energy information helped enhance the image quality by eliminating multiple scattering events in the imaging object.

DOI: [10.1103/PhysRevApplied.22.024049](https://doi.org/10.1103/PhysRevApplied.22.024049)

I. INTRODUCTION

Positron emission tomography (PET) is one of the most unrivaled imaging modalities in nuclear medicine and has been extensively used for the diagnosis of life-threatening diseases, such as cancer. In PET measurements, positron-labeled radiopharmaceuticals, such as ^{18}F -fluorodeoxyglucose are injected into patients as a tracer, and the two back-to-back 511-keV γ rays produced following positron-electron annihilation are measured by detectors surrounding the patients arranged on a cylindrical shape. The measured data are then processed using tomographic image reconstruction algorithms, and cross-section images are obtained. Unlike most imaging modalities in nuclear medicine, PET requires the coincident detection of a pair of γ rays, indicating that additional information, such as the time-of-flight (TOF) between the γ -ray pair, can be obtained on an event-by-event basis. TOF information can locally constrain the position of annihilation in the body and improve the quality of events. Consequently, the SNR of PET images can be enhanced according to the following equation:

$$\text{SNR}_{\text{TOF}} = \sqrt{\frac{D}{c \times \Delta t}} \text{SNR}_{\text{non-TOF}}, \quad (1)$$

*Contact author: yuya.onishi@hpk.co.jp

†Contact author: ryosuke.ota@crl.hpk.co.jp

where D , c , and Δt denote the patient diameter, speed of light, and coincidence time resolution (CTR) [1]. Therefore, a better temporal resolution can increase the SNR of PET images. Accordingly, researchers have been enthusiastically dedicated to the development of PET detectors with high-timing precision [2].

When the CTR is improved down to 30-ps FWHM, the spatial localization along the line-of-response between detectors yielded an 4.5-mm FWHM, which almost corresponds to the spatial resolution of commercially available PET scanners. This indicates that signal sources can be directly localized in three-dimensional space using ultrafast TOF information on an event-by-event basis, and it is possible to circumvent dedicated image-reconstruction processes, which tend to be time consuming and noise amplifying, to generate cross-section images. Furthermore, the elimination of image-reconstruction processes frees us from the geometric constraints of traditional ring-shaped PET scanners, thus allowing the realization of an arbitrary scanner size and shape. This has been discussed more than 40 years ago by Budinger [3].

Owing to the recent deeper understanding of the physics of γ -ray detection including interactions with luminescent materials, light transportation, photodetectors, and signal processing [4–7], detectors with an approximate CTR of 30-ps FWHM have been developed [8–10]. In addition, it has been reported that deep learning techniques can be applied to improve the timing performance of detectors

[11,12]. By combining fast materials and deep learning, the first experimental validation of reconstruction-free positron emission imaging was demonstrated [13] and named direct positron emission imaging (dPEI). In Ref. [13], attenuation correction was performed manually on the generated dPEI image to correct attenuations of γ rays in the objects and accurately quantify the accumulated tracers, as the three-dimensional material components of the objects were known. Therefore, in the future clinical situations, imaging methods compatible with dPEI should be developed to provide the anatomical information of imaging objects required for attenuation correction.

In this context, a Compton scattering-based reconstruction-free anatomical imaging method was proposed [14]. In this method, a pair of detector panels are located face-to-face, and an imaging object is located at the center of the detector panels, as shown in Fig. 1(a). This geometry can maintain dPEI's potential, which is freed from any geometric constraints and can thus be compact. An external positron-emitting source is located between the object and the detector panel. Annihilation γ rays are detected by detectors; however, one of the γ rays undergoes Compton scattering in the object. Given that the probability of Compton scattering is proportional to the electron density, a three-dimensional electron-density map, which is equivalent to the anatomical information of the object, can be constructed without image-reconstruction processes by directly localizing the Compton scattering positions using ultrafast TOF information. In principle, the Compton scattering positions \mathbf{C} can be algebraically solved when the external source position \mathbf{S} and the detected

positions \mathbf{r} and \mathbf{R} of the two dPEI detectors are known subject to the following constraints:

$$|\mathbf{C} - \mathbf{S}| + |\mathbf{C} - \mathbf{R}| - |\mathbf{r} - \mathbf{S}| = \Delta t \times c, \quad (2)$$

$$\text{such that } \mathbf{r} - \mathbf{S} // \mathbf{C} - \mathbf{S}. \quad (3)$$

However, Ref. [14] solved approximately Eqs. (2) and (3) using Newton's iterative root-finding algorithm owing to its complexity. The performance in terms of spatial resolution of the generated anatomical images is not fully understood.

In this study, we provide the exact solution by algebraically solving Eq. (2). Once the exact solution is obtained, the system performance can be quantitatively estimated via total differentiation. By estimating system performance, we can conclude the type of physical events that will deteriorate system performance. Finally, we validated our theoretical predictions using Monte Carlo simulations.

II. METHODS

A. Algebraic solution

In this section, the algebraic solutions of Eq. (2) are derived by assuming that the external source position corresponds to the origin $\mathbf{S} = (0, 0, 0)$. This coordinate shift and approximation simplify Eq. (2); therefore, Eq. (2) can be rewritten as

$$|\mathbf{C}| + |\mathbf{C} - \mathbf{R}| - |\mathbf{r}| = L, \quad (4)$$

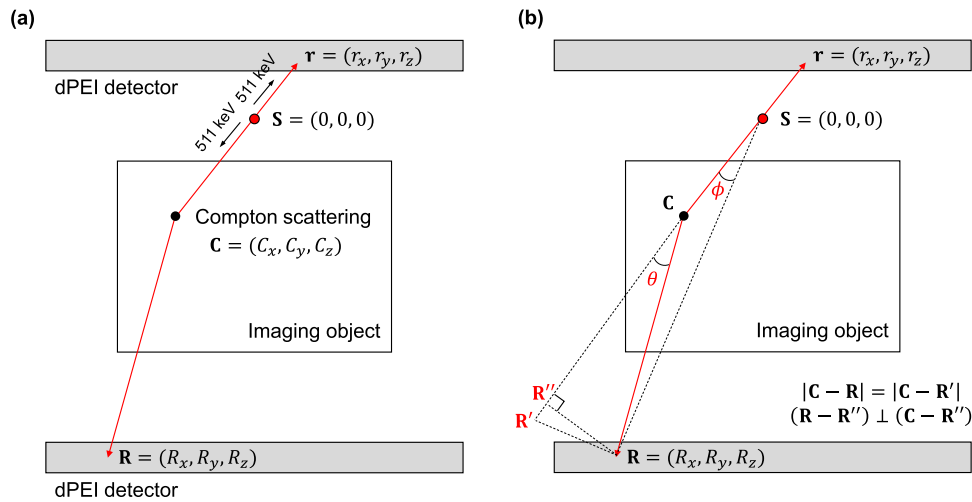


FIG. 1. (a) Schematic view of the reconstruction-free anatomical imaging method based on Compton scattering and definitions of parameters used in this study. A pair of direct positron emission imaging (dPEI) detectors with high spatiotemporal resolution are located face-to-face, and an imaging object is located between two detectors. An external positron emitting source \mathbf{S} is located between the imaging object and one dPEI detector. Using the spatiotemporal information of dPEI detectors, the Compton scattering positions \mathbf{C} , which offer anatomical information of the imaging object, are calculated on an event-by-event basis. (b) Supporting dotted black lines and other parameters used to make the Eq. (9) more physically intuitive. The parameter θ can be considered as the Compton scattering angle. By introducing θ , Eq. (9) can be rewritten to Eq. (16).

where L is $\Delta t \times c$; furthermore, Eq. (3) can be rewritten as,

$$\mathbf{C} \times \mathbf{r} = \mathbf{0}. \quad (5)$$

Here, $C_x/r_x < 0$ owing to the antiparallel condition of the annihilation γ rays. Consequently, the Compton scattering position $C_{\mu=x,y,z}$ is solved.

$$C_{\mu} = \frac{r_{\mu}}{2} \times \frac{R^2 - (L+r)^2}{\mathbf{r} \cdot \mathbf{R} + r(L+r)}. \quad (6)$$

When an algebraic solution is defined, its total differentiation can also be defined.

$$dC_{\mu} = \sum_{v=x,y,z} \frac{\partial C_{\mu}}{\partial r_v} dr_v + \sum_{v=x,y,z} \frac{\partial C_{\mu}}{\partial R_v} dR_v + \frac{\partial C_{\mu}}{\partial L} dL. \quad (7)$$

In this case, $dr_{v=x,y}$, $dr_{v=z}$, and dL are the xy spatial, depth of interaction, and spatial resolutions derived from CTR, respectively. According to the error propagation law, the estimated spatial resolution $\Delta C_{\mu=x,y,z}$ is

$$\Delta C_{\mu} = \left(\sum_{v=x,y,z} \left(\frac{\partial C_{\mu}}{\partial r_v} dr_v \right)^2 + \sum_{v=x,y,z} \left(\frac{\partial C_{\mu}}{\partial R_v} dR_v \right)^2 + \left(\frac{\partial C_{\mu}}{\partial L} dL \right)^2 \right)^{1/2}. \quad (8)$$

We can now calculate all partial differentiations. Henceforth, we focus only on C_x given the symmetry of x, y , and z components in the equation.

$$\frac{\partial C_x}{\partial L} = -\frac{r_x (L+r)^2 r + 2(L+r) \mathbf{r} \cdot \mathbf{R} + R^2 r}{2 (\mathbf{r} \cdot \mathbf{R} + r(L+r))^2}, \quad (9)$$

$$\frac{\partial C_x}{\partial R_x} = \frac{r_x (L+r)^2 r_x + 2(L+r) R_x r + 2R_x \mathbf{r} \cdot \mathbf{R} - R^2 r_x}{2 (\mathbf{r} \cdot \mathbf{R} + r(L+r))^2}, \quad (10)$$

$$\frac{\partial C_x}{\partial R_y} = \frac{r_x (L+r)^2 r_y + 2(L+r) R_y r + 2R_y \mathbf{r} \cdot \mathbf{R} - R^2 r_y}{2 (\mathbf{r} \cdot \mathbf{R} + r(L+r))^2}, \quad (11)$$

$$\frac{\partial C_x}{\partial R_z} = \frac{r_x (L+r)^2 r_z + 2(L+r) R_z r + 2R_z \mathbf{r} \cdot \mathbf{R} - R^2 r_z}{2 (\mathbf{r} \cdot \mathbf{R} + r(L+r))^2}, \quad (12)$$

$$\frac{\partial C_x}{\partial r_x} = \frac{1}{(\mathbf{r} \cdot \mathbf{R} + r(L+r))^2} \left[(L+r)^3 \left(\frac{r_x^2}{r} - r \right) + (L+r)^2 (r_x (R_x + r_x) - 2r_x^2 - \mathbf{r} \cdot \mathbf{R}) + (L+r) \left(R^2 r - \frac{r_x^2}{r} (2\mathbf{r} \cdot \mathbf{R} + R^2) \right) + R^2 (\mathbf{r} \cdot \mathbf{R} - r_x (R_x + r_x)) \right], \quad (13)$$

$$\frac{\partial C_x}{\partial r_y} = \frac{r_x (L+r)^3 \frac{r_y}{r} + (L+r)^2 (R_y - r_y) + (L+r) (2\mathbf{r} \cdot \mathbf{R} + R^2) \frac{r_y}{r} - R^2 (R_y + r_y)}{2 (\mathbf{r} \cdot \mathbf{R} + r(L+r))^2}, \quad (14)$$

$$\frac{\partial C_x}{\partial r_z} = \frac{r_x (L+r)^3 \frac{r_z}{r} + (L+r)^2 (R_z - r_z) + (L+r) (2\mathbf{r} \cdot \mathbf{R} + R^2) \frac{r_z}{r} - R^2 (R_z + r_z)}{2 (\mathbf{r} \cdot \mathbf{R} + r(L+r))^2}. \quad (15)$$

Thus, ΔC_x can be calculated quantitatively and numerically, and a quantitative estimation of the spatial resolution is possible. Nonetheless, it is difficult to draw general conclusions on the spatial resolution because the parameters nonlinearly couple with each other. However, in only the case of $\partial C_x / \partial L$, we can make Eq. (9) easier and more physically intuitive by introducing the parameters \mathbf{R}' , \mathbf{R}'' , and θ , as shown Fig. 1(b). Parameter θ can be considered as the Compton scattering angle. Regarding Eq. (4) and the law of cosines for $\triangle SRR'$, the numerator in Eq. (9) is $|\mathbf{R} - \mathbf{R}'|^2 r$. Furthermore, the denominator in Eq. (9) is $|\mathbf{R}' - \mathbf{R}''|^2 r^2$. Eventually, Eq. (9) can be rewritten as

$$\frac{\partial C_x}{\partial L} = -\frac{r_x}{r} \frac{1}{1 - \cos \theta}. \quad (16)$$

Herein, we used $\angle RR'R'' = (\pi - \theta)/2$ and the double angle formula. Although θ is a function of $\phi(\mathbf{r}, \mathbf{R})$ because θ should always be larger than ϕ , θ is a unique parameter that can independently control L . Equation (16) suggests that events in which $\cos \theta$ is close to one drastically increase the spatial uncertainty and should be discarded. In other words, the forward Compton scattering events should be discarded to maintain the spatial resolution of the imaging method proposed in Ref. [14]. In this imaging method, this type of Compton scattering event can be easily discriminated using the energy information of the scatter-side detector, which was not used in the previous study.

The availability of energy information also has the potential to eliminate events with multiple Compton scattering within the object and events that are not photoelectrically absorbed within the detector (Fig. 2). Specifically,

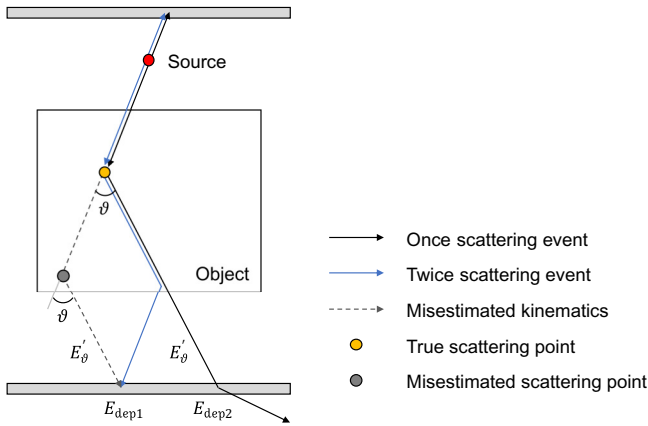


FIG. 2. Examples of events to be discriminated using energy information of the scatter-side detector. The energy E'_θ from the misestimated position with θ owing to multiple (e.g., twice) scattering is outside the $E_{\text{dep}1} \pm 2\sigma$ range and is eliminated. As the energy deposit is reduced by scattering and escaping from the detector, the energy E'_θ after a single scattering is outside the $E_{\text{dep}2} \pm 2\sigma$ range and is eliminated.

we can compare the recorded energy deposit E_{dep} of the γ rays reaching the scatter-side detector with the energy E'_θ derived from the scattering angle of that event because the θ and energy deposit can be independently measured on an event-by-event basis. Subsequently, we discriminated events outside the $E_{\text{dep}} \pm 2\sigma$, where σ is the standard deviation of a Gaussian distribution with a certain energy resolution. The energy derived from the Compton scattering angle of the annihilation γ rays is expressed as follows:

$$E'_\theta = \frac{E_\gamma}{1 + \frac{E_\gamma}{m_0 c^2} (1 - \cos \theta)}, \quad (17)$$

where E_γ is the initial γ energy (511 keV) and $E_\gamma / m_0 c^2 = 1$.

B. Monte Carlo simulations

Monte Carlo simulations were performed to validate our theory using Geant4 (version 11.0) [15]. The simulation setup is shown in Fig. 3. The bismuth-germanate (BGO)-based detectors were placed face to face. A water-filled phantom embedded six cavities with different sizes (from 8 to 22 mm ϕ) for spatial resolution evaluation was placed between two detectors. The large cavities (18 and 22 mm ϕ) consisted of bone, whereas the small cavities (8, 10, 12, and 14 mm ϕ) consisted of air. The distances between the cavities with the same diameter were the same as their diameters. An external positron-emitting source with an infinitesimal size was set between one of the

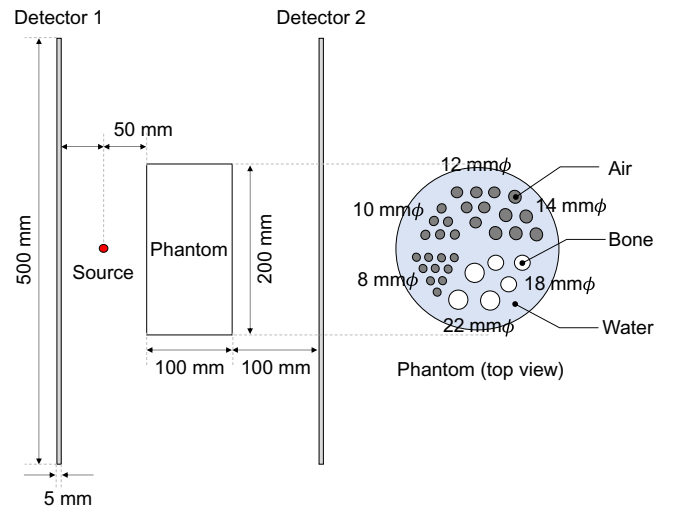


FIG. 3. Experimental setup for the Monte Carlo simulations based on Geant4. A phantom is placed between two BGO-based detectors for spatial resolution evaluation. Six different sizes of cavities with 8, 10, 12, 14, 18, and 22 mm ϕ were embedded in the phantom. A positron emission point source is located between one of the detectors and the phantom.

detectors and the phantom. In the Monte Carlo simulations, the position and time of the interaction and energy deposition on the detectors were recorded event by event, and optical photons were not generated. After recording the information, the time and position of the interaction and energy deposition were blurred as intrinsic detector performances. The spatial resolution of the detectors was supposed to be isotropic $3 \times 3 \times 3 \text{ mm}^3$ FWHM, whereas the CTR was varied from 30- to 200-ps FWHM. The energy resolution was considered as 13% FWHM according to Ref. [16]. All the simulations were performed with 5×10^8 annihilations.

To confirm the improvement in spatial resolution by discarding events with small Compton scattering angles, the recorded events were classified into two categories based on the energy spectrum such that each category had almost the same number of events. For example, the energy windows of the two categories were separated at 390 keV in the case of the CTR of 30-ps FWHM. In this study, we made the counts almost the same to use more of the obtained events as a criterion for setting the energy threshold. Selecting a lower-energy threshold within the limits permitted by the system geometry can improve the spatial resolution of the images. Because the uniformity of the generated image worsens by applying this energy threshold, the anatomical image generated after energy selection

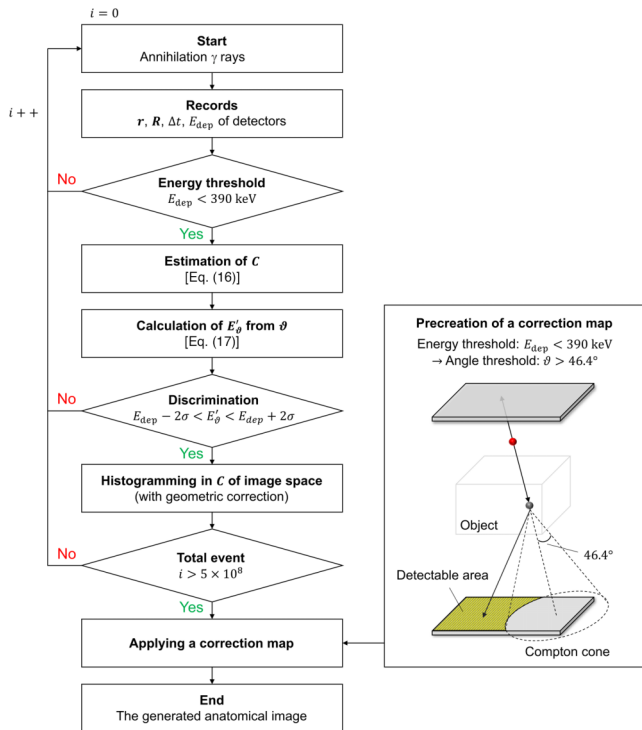


FIG. 4. Flowchart of event selection in the proposed reconstruction-free anatomical imaging algorithm and a conceptual diagram for precreating a correction map. The E_{dep} threshold of 390 keV corresponds to a CTR of 30 ps FWHM.

requires correction. A correction was applied to all voxels in the image by precreating a correction map based on the area of the detector that intersected the Compton cone, with the cone angle determined based on the selected energy window (EW). Figure 4 presents a conceptual diagram of this correction map and summarizes the overall flowchart of event selection in the proposed imaging algorithm. The generated images are represented by $128 \times 128 \times 128$ voxels with dimension of $2.19 \times 2.19 \times 2.19 \text{ mm}^3$.

III. RESULTS

We obtained reconstruction-free anatomical images based on Compton scattering positions, which were calculated algebraically. The discrimination of multiple scattering events using energy information was first performed, and the improvement in the spatial resolution of the generated images was validated by applying an energy threshold.

Figure 5 shows the energy histogram of the scatter-side detector with and without multiple scattering discrimination using energy information for a CTR of 30 ps. Table I shows the ratio of the number of Compton scattering times to the total events shown in the energy histogram. The ratios without discrimination once, twice, three times, and four times were 0.544, 0.253, 0.114, and 0.050, respectively, whereas the ratios with discrimination were 0.828, 0.141, 0.024, and 0.005, respectively. From these results, it was possible to eliminate events with multiple Compton scattering within the phantom and events that were not photoelectrically absorbed within the detector by discrimination based on energy information; the ratio of single

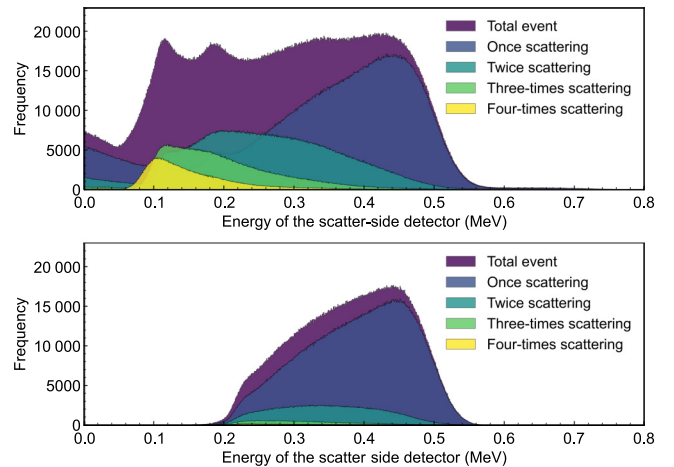


FIG. 5. Energy histogram on the scatter-side detector (a) without and (b) with multiple scattering discrimination using energy information at a coincidence time resolution (CTR) of 30 ps. Each color represents the number of Compton scattering times within the phantom.

TABLE I. Ratio of the number of the Compton scattering times in total event without and with multiple scattering discrimination at a CTR of 30 ps corresponding to the energy histogram in Fig. 5. Energy information provides significant elimination of multiple scattering events, which decrease the spatial performance of the generated images.

Number of scattering events	w/o discri.	w/ discri.
Once	0.544	0.828
Twice	0.253	0.141
Three times	0.114	0.024
Four times	0.050	0.005

scattering events to total events increased by 28.4% from 55.4% to 82.8%.

Figure 6 shows the generated Compton scattering-based reconstruction-free images and their line profiles with and

without energy selection at different CTR values (ranging from 30 to 200 ps). The energy window for each CTR condition was set such that the number of counts within the two categories was almost the same. The displayed images were summed across all slices to suppress statistical noise and normalized to the same grayscale value. The spatial resolution of the image was evaluated using line profiles traversing the 8 and 12 mm ϕ cavities. The percentages of events used for image formation with energy below 390 (30 ps), 380 (50 ps), 370 (75 ps), 370 (100 ps), and 340 keV (200 ps) were 0.49%, 0.44%, 0.40%, 0.39%, and 0.26% of the total annihilation events, respectively. As indicated by red arrows in Fig. 6, the spatial resolution of the generated image was significantly improved by selecting events with lower energy than 390 or 380 keV (large Compton scattering angle) in the scatter-side detector, whereas the resolution was degraded by selecting events with higher

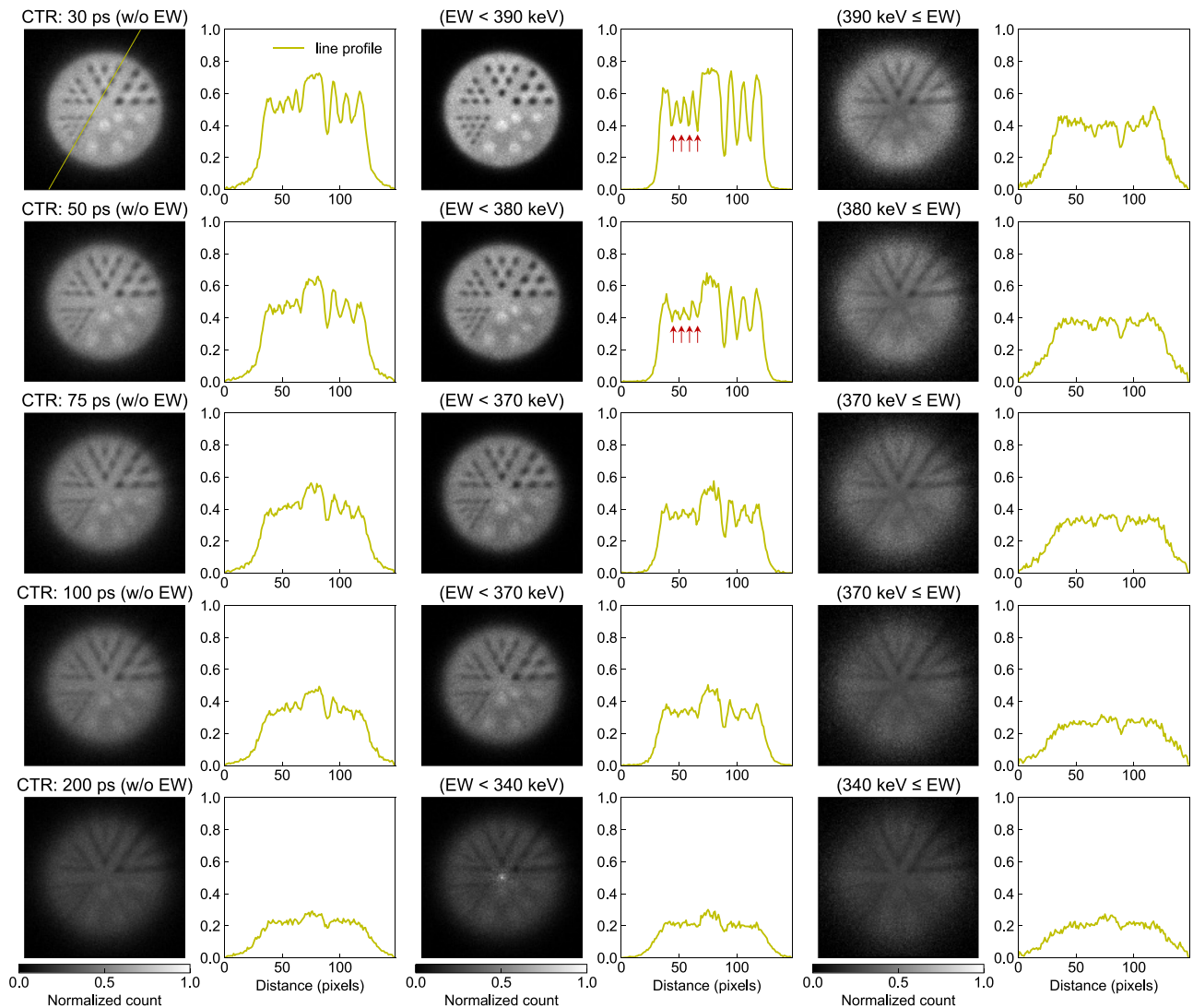


FIG. 6. Generated images and their line profiles (left) without and (middle and right) with energy windows (EWs) at different CTR values (ranging from 30 to 200 ps). The spatial resolution of the generated image was improved by selecting events with low energy in the scatter-side detector as indicated by the red arrows, and was degraded by selecting high-energy events.

energy than 390 or 380 keV (small Compton scattering angle). This result is consistent with the interpretation of Eq. (16) derived from an algebraic solution. With the system geometry in this simulation, the use of energy information allowed us to observe the smallest 8 mm ϕ cavities and separate different materials in the phantom, such as air, water, and bone, under detector conditions with a CTR of 50 ps and a detector spatial resolution of 3 mm [17].

IV. DISCUSSION

In this study, we provided an exact solution by algebraically solving the Compton scattering positions, which were solved approximately in the reconstruction-free anatomical imaging method proposed in a previous study [14]. Based on the exact solution, we found that the difference in the path lengths of the annihilation γ rays, which is described as a function of the Compton scattering angle, had the greatest effect on the spatial resolution of the generated images. Even if the CTR is much better than 30 ps, the total resolution ΔC_μ of Eq. (8) diverges unless the image includes events with small Compton scattering angles. The reason why the image quality was worse than the intrinsic detector resolution of a CTR of 10 ps and an xyz resolution of 1 mm in Ref. [14] was ascribed to events with small Compton scattering angles owing to the system geometry. The spatial resolution of the generated images was improved by setting an energy threshold to exclude such events (Fig. 6), thus allowing us to observe the smallest cavities even with detector conditions of a CTR of 50 ps and a detector spatial resolution of 3 mm. A CTR of approximately 30 ps with a microchannel plate photomultiplier tube (MCP PMT) has already been achieved [13]. BGO-based MCP PMT, which are possible candidates for integration into the MCP PMT structure, can provide energy information, thus making this imaging algorithm practical. Achieving such ultimate time and energy resolution allows for the effective use of various scattering events in nuclear medicine imaging. It has been shown that PET imaging can provide spatial information on the source position even after scattering, which allows the reconstruction of scattered photons [18]. Moreover, this study proposed another concept for obtaining the anatomical images of an object without image reconstruction through the installation of an external positron source.

The use of energy information is also helpful in eliminating multiple scattering events in an object, whereas a previous study [14] targeted only single scattering events *a priori*. In addition, it was possible to eliminate events that escaped from the detector, as shown in the low-energy region of Fig. 5(a), which improved the SNR of the generated images. Intercrystal scattering, which is a type of Compton scattering of photons from one crystal to adjacent crystals, in the detector was not considered in this

study. Although multiple scattering events remain, using other dense materials with better energy resolution than BGO, such as thallium bromide [19], is an alternative for eliminating multiple scattering events.

Although the energy window was set at 390 keV such that the number of counts within the two categories was almost the same in this study, a lower energy threshold would provide better spatial resolution according to Eq. (16). However, their energy thresholds are limited by their geometric structures. This is because the scattering angle limitation due to energy selection arises in areas where events are not geometrically detected. For example, in the case of an event scattered at the top center of the phantom, the scattering angle should be less than 60.5° for detections by the scatter-side detector, which requires an energy deposit higher than 338.9 keV. Therefore, if the energy threshold is lower than this value, it is impossible to detect events in the area and properly correct for nonuniform count distributions in the generated image. The cause of the hotspot at the center of the image with EW <340 keV at a CTR of 200 ps in Fig. 6 is also attributed to this reason. A simple strategy for solving this challenge is to widen the scatter-side detector panel. Alternatively, the system geometry needs to be optimized to detect events with larger scattering angles. The design of the geometry will depend on the applications. Correspondingly, it will be useful to conduct additional studies to devise ways to fill the gap between the ideal and actual performance.

We acknowledge that this study has several limitations that should be addressed to make the proposed method feasible. First, a strong link exists between energy deposit and CTR. For typical scintillation photons, the CTR normally depends on the deposited energy, that is, lower energy deposits from Compton interactions have worse CTR. In this study, when a CTR was selected, then the value was fixed for all energies whereas one could expect a CTR degradation approximately proportional to $1/\sqrt{\text{Energy}}$ [9]. On the other hand, we envision obtaining timing information using Cherenkov photons. In this case, a CTR of 30 ps will be realized by achieving a single-photon time resolution of $30/\sqrt{2}$, regardless of the energy if the photon time spread in a crystal is ignored. The lower energy considerably reduces the detection efficiency rather than the CTR because only approximately one Cherenkov photon can be detected. For instance, for a 511-keV γ ray, approximately 17 Cherenkov photons are produced in BGO upon photopeak interaction with a photoelectron energy of 511 minus K -shell binding energy being equal to 420 keV. If the energy is lowered to 390 keV, approximately 10 Cherenkov photons would be produced because of nonlinearities. Ultimately, an extremely small number of Cherenkov photons can be detected in such an energy region. Events with no Cherenkov photon detection would degrade image quality because of a broad CTR based on scintillation events. Therefore, more counts would be

required to obtain image quality similar to that in this study. Furthermore, this study indicated the significance of energy discrimination capability. However, such energy discrimination capability is yet to be achieved with pure Cherenkov radiators and MCP PMTs. Although some type of energy information could be available [20,21], this energy discrimination is a disadvantage for this study, as the study favors events with high-energy deposition. Although we envision the BGO-based MCP PMT could provide energy information as a possible candidate for dPEI, the good timing and energy capability still need to be demonstrated. The current timing resolution is insufficient for the proposed method, even with Cherenkov and scintillation classification techniques [22,23]. Moreover, we adopted an energy resolution of 13%, a value based on a previous study [16]; however, this value can depend on several factors (detector geometry, surface conditions, readout, energy itself, etc.). The degradation of the time and energy resolution affects the quality of the generated images. Because this study promotes a theoretical understanding of the Compton scattering-based reconstruction-free anatomical imaging method, future studies should evaluate under realistic detector conditions.

The validation results demonstrate the effectiveness of this reconstruction-free anatomical imaging method. The realization of the whole reconstruction-free imaging combining this method with dPEI offers the same compact and flexible geometry and is expected to have synergistic effects on each modality. These hybrid images with anatomical information obtained from the proposed imaging technique and functional information obtained from dPEI may provide a more accurate diagnosis and have great potential for attenuation correction in dPEI images. This makes it possible to evaluate quantitatively the biodistribution of tracers and their therapeutic effects in almost real time.

V. CONCLUSION

This study introduced a theoretical understanding of the Compton scattering-based reconstruction-free anatomical

imaging method and the simulation results that support it. First, we provided an exact solution by algebraically solving for the Compton scattering positions. When the exact solution was obtained, system performance was quantitatively estimated via total differentiation. We found that the difference in the path lengths of the annihilation γ rays, which is a function of the Compton scattering angle, had the greatest effect on the spatial resolution of the generated image. Monte Carlo simulations showed that the spatial resolution of the generated images was improved by selecting events with large Compton scattering angles by applying an energy threshold, which is consistent with the theory derived from an algebraic solution. Furthermore, the use of energy information helps eliminate multiple scattering events in the imaging object. These hybrid images with anatomical and functional information may provide a more accurate diagnosis and have the potential for attenuation correction in dPEI.

ACKNOWLEDGMENTS

The authors would like to thank the scientific advice provided by Mr. Kibo Ote, Mr. Fumio Hashimoto, and the members of the Fifth Research Group at the Central Research Laboratory of Hamamatsu Photonics K.K.

APPENDIX A: DERIVATION OF THE ALGEBRAIC SOLUTION

This section details the procedure for deriving the algebraic solution [Eq. (6)] of the Compton scattering position. From the definition of cross product, Eq. (5) can be expressed as

$$C_x r_y - C_y r_x = 0, \quad (\text{A1})$$

$$C_y r_z - C_z r_y = 0, \quad (\text{A2})$$

$$C_z r_x - C_x r_z = 0. \quad (\text{A3})$$

Using these equations, Eq. (4) can be rewritten as follows:

$$\sqrt{C_x^2 + C_y^2 + C_z^2} + \sqrt{(C_x - R_x)^2 + (C_y - R_y)^2 + (C_z - R_z)^2} = L + |\mathbf{r}|, \quad (\text{A4})$$

$$-\frac{|\mathbf{r}|}{r_x} C_x + \sqrt{(C_x - R_x)^2 + \left(\frac{r_y}{r_x} C_x - R_y\right)^2 + \left(\frac{r_z}{r_x} C_x - R_z\right)^2} = L + |\mathbf{r}|. \quad (\text{A5})$$

We added a minus sign at the first term on the left side of Eq. (A5) because of $C_x/r_x < 0$ derived from the antiparallel condition of the annihilation γ rays. Finally, Eq. (6) can be obtained by solving Eq. (A5) for C .

APPENDIX B: AN ADDITIONAL ALGEBRAIC SOLUTION

In Sec. II A, the algebraic solution was calculated based on the law of cosine; however, in this Appendix, another algebraic solution is demonstrated. Considering the sine rule for $\triangle SCR$, $|C|$ and $|C - R|$ can be expressed as follows,

$$|C| = |R| \frac{\sin(\theta - \phi)}{\sin \theta}, \quad (B1)$$

$$|C - R| = |R| \frac{\sin \phi}{\sin \theta}. \quad (B2)$$

By combining these with Eq. (4), Eq. (9) can be expressed as a function of θ and ϕ as

$$\frac{\partial C_x}{\partial L} = -\frac{r_x r R^2 \frac{(\sin \phi + \sin(\theta - \phi))^2}{\sin^2 \theta} - 2r R^2 \cos \phi \frac{\sin \phi + \sin(\theta - \phi)}{\sin \theta} + r R^2 \sin^2 \theta}{\left(-r R \cos \phi + r R \frac{\sin \phi + \sin(\theta - \phi)}{\sin \theta}\right)^2}. \quad (B3)$$

By carefully unfolding Eq. (B3), the same result as Eq. (16) can be obtained.

- [1] M. Conti, Focus on time-of-flight pet: The benefits of improved time resolution, *Eur. J. Nucl. Med. Mol. Imaging* **38**, 1147 (2011).
- [2] P. Lecoq, C. Morel, J. O. Prior, D. Visvikis, S. Gundacker, E. Auffray, P. Križan, R. M. Turtos, D. Thers, E. Charbon *et al.*, Roadmap toward the 10 ps time-of-flight pet challenge, *Phys. Med. Biol.* **65**, 21RM01 (2020).
- [3] T. F. Budinger, Time-of-flight positron emission tomography: Status relative to conventional pet, *J. Nucl. Med.* **24**, 73 (1983).
- [4] P. Lecoq, M. Korzhik, and A. Vasiliev, Can transient phenomena help improving time resolution in scintillators?, *IEEE Trans. Nucl. Sci.* **61**, 229 (2013).
- [5] S. Gundacker, E. Auffray, K. Pauwels, and P. Lecoq, Measurement of intrinsic rise times for various L(Y)SO and LuAG scintillators with a general study of prompt photons to achieve 10 ps in TOF-PET, *Phys. Med. Biol.* **61**, 2802 (2016).
- [6] P. Lecoq, Pushing the limits in time-of-flight pet imaging, *IEEE Trans. Radiat. Plasma. Med. Sci.* **1**, 473 (2017).
- [7] R. Ota, Photon counting detectors and their applications ranging from particle physics experiments to environmental radiation monitoring and medical imaging, *Radiol. Phys. Technol.* **14**, 134 (2021).
- [8] R. Ota, K. Nakajima, I. Ogawa, Y. Tamagawa, H. Shimoi, M. Suyama, and T. Hasegawa, Coincidence time resolution of 30 ps FWHM using a pair of Cherenkov-radiator-integrated MCP-PMTs, *Phys. Med. Biol.* **64**, 07LT01 (2019).
- [9] S. Gundacker, R. Turtos, N. Kratochwil, R. Pots, M. Paganoni, P. Lecoq, and E. Auffray, Experimental time resolution limits of modern SIPMS and TOF-PET detectors exploring different scintillators and Cherenkov emission, *Phys. Med. Biol.* **65**, 025001 (2020).
- [10] R. Ota, K. Nakajima, I. Ogawa, Y. Tamagawa, S. Kwon, E. Berg, S. Cherry, H. Shimoi, Y. Hasegawa, H. Nishizawa

- et al.*, Lead-free MCP to improve coincidence time resolution and reduce MCP direct interactions, *Phys. Med. Biol.* **66**, 064006 (2021).
- [11] E. Berg and S. R. Cherry, Using convolutional neural networks to estimate time-of-flight from PET detector waveforms, *Phys. Med. Biol.* **63**, 02LT01 (2018).
 - [12] Y. Onishi, F. Hashimoto, K. Ote, and R. Ota, Unbiased TOF estimation using leading-edge discriminator and convolutional neural network trained by single-source-position waveforms, *Phys. Med. Biol.* **67**, 04NT01 (2022).
 - [13] S. I. Kwon, R. Ota, E. Berg, F. Hashimoto, K. Nakajima, I. Ogawa, Y. Tamagawa, T. Omura, T. Hasegawa, and S. R. Cherry, Ultrafast timing enables reconstruction-free positron emission imaging, *Nat. Photonics* **15**, 914 (2021).
 - [14] Y. Onishi, F. Hashimoto, K. Ote, and R. Ota, Whole reconstruction-free system design for direct positron emission imaging from image generation to attenuation correction, *IEEE Trans. Med. Imaging* **43**, 5 (2023).
 - [15] S. Agostinelli, J. Allison, K. a. Amako, J. Apostolakis, H. Araujo, P. Arce, M. Asai, D. Axen, S. Banerjee, G. Barand *et al.*, GEANT4—a simulation toolkit, *Nucl. Instrum. Methods Phys. Res. A* **506**, 250 (2003).
 - [16] S. Brunner and D. Schaart, BGO as a hybrid scintillator/Cherenkov radiator for cost-effective time-of-flight PET, *Phys. Med. Biol.* **62**, 4421 (2017).
 - [17] L. Chen, L. Ma, G. Huang, Z. Hua, M. Jin, Z. Jin, S. Qian, L. Ren, S. Si, J. Sun *et al.*, Coincidence time resolution of 50 ps FWHM using a pair of multi-anode MCP-PMTs with Cherenkov radiator window, *Nucl. Instrum. Methods Phys. Res. A* **1062**, 169173 (2024).
 - [18] M. Conti, I. Hong, and C. Michel, Reconstruction of scattered and unscattered PET coincidences using TOF and energy information, *Phys. Med. Biol.* **57**, N307 (2012).
 - [19] K. Hitomi, C. Kim, M. Nogami, K. Shimazoe, and H. Takahashi, Characterization of coincidence time resolutions of $TlBr_xCl_{1-x}$ crystals as Cherenkov radiators, *Jpn. J. Appl. Phys.* **62**, 081001 (2023).
 - [20] N. Kratochwil, S. Gundacker, and E. Auffray, A roadmap for sole Cherenkov radiators with SIPMS in TOF-PET, *Phys. Med. Biol.* **66**, 195001 (2021).

- [21] G. Razdevšek, R. Pestotnik, P. Križan, S. Korpar, D. Consuegra, A. Seljak, A. Studen, and R. Dolenc, Exploring the potential of a Cherenkov TOF pet scanner: A simulation study, *IEEE Trans. Radiat. Plasma. Med. Sci.* **7**, 52 (2013).
- [22] N. Kratochwil, S. Gundacker, P. Lecoq, and E. Auffray, Pushing Cherenkov PET with BGO via coincidence time resolution classification and correction, *Phys. Med. Biol.* **65**, 115004 (2020).
- [23] S. Kwon, E. Roncali, A. Gola, G. Paternoster, C. Piemonte, and S. Cherry, Dual-ended readout of bismuth germanate to improve timing resolution in time-of-flight PET, *Phys. Med. Biol.* **64**, 105007 (2019).